Nanoscale 5.11 (2013): 4729-4736

DOI: https://doi.org/10.1039/c3nr34088k

Nanoscale

RSC Publishing

PAPER

Mapping *in vitro* local material properties of intact and disrupted virions at high resolution using multi-harmonic atomic force microscopy†

Cite this: DOI: 10.1039/c3nr34088k

Alexander Cartagena,‡[a] Mercedes Hernando-Pérez,‡[b] José L. Carrascosa,[c] Pedro J. de Pablo*[b] and Arvind Raman*[a]

Received 13th December 2012
Accepted 21st March 2013

DOI: 10.1039/c3nr34088k

www.rsc.org/nanoscale

Understanding the relationships between viral material properties (stiffness, strength, charge density, adhesion, hydration, viscosity, *etc.*), structure (protein sub-units, genome, surface receptors, appendages), and functions (self-assembly, stability, disassembly, infection) is of significant importance in physical virology and nanomedicine. Conventional Atomic Force Microscopy (AFM) methods have measured a single physical property such as the stiffness of the entire virus from nano-indentation at a few points which severely limits the study of structure–property–function relationships. We present an *in vitro* dynamic AFM technique operating in the intermittent contact regime which synthesizes anharmonic Lorentz-force excited AFM cantilevers to map quantitatively at nanometer resolution the local electro-mechanical force gradient, adhesion, and hydration layer viscosity *within* individual ϕ29 virions. Furthermore, the changes in material properties over the entire ϕ29 virion provoked by the local disruption of its shell are studied, providing evidence of bacteriophage depressurization. The technique significantly generalizes recent multi-harmonic theory (A. Raman, *et al.*, *Nat. Nanotechnol.*, 2011, **6**, 809–814) and enables high-resolution *in vitro* quantitative mapping of multiple material properties *within* weakly bonded viruses and nanoparticles with complex structure that otherwise cannot be observed using standard AFM techniques.

Introduction

Viruses are striking examples of macromolecular nano-machines which carry out complex functions with minimalistic structure.[1] Understanding the relationships between viral material properties (stiffness, strength, charge density, adhesion, hydration, viscosity, *etc.*), structure (protein sub-units, genome, surface receptors, appendages), and functions (self-assembly, stability, disassembly, infection) is of significant importance in physical virology and nanomedicine,[2–8] for designing nano-containers[9] and synthetic virus-like particles,[10] and for the templated assembly of nanomaterials.[11–13] Standard AFM techniques based on nano-indentation have measured single physical property (stiffness) of individual viruses at few points, but they lack spatial and temporal resolution.[3,5,14,15] However, key to unraveling the structure–property–function relationships of viruses is the ability to quantitatively map the spatial variation of multiple local material properties *within* an individual viral particle under physiological conditions – a challenging goal for conventional AFM methods.

Viruses are relatively stiff and often icosahedral particles. As a result isolated viruses only bind weakly to substrates over small contact areas and can be easily removed by the lateral forces applied to the particle if the AFM tip is in continuous contact with the particle while scanning.[16] Intermittent contact can be achieved through the pointwise acquisition of static force–distance curves or through its variants.[17,18] However at present these methods require great care to reduce forces at the edges of weakly bonded isolated particles and have rarely been used to map properties within individual viruses.[19] Conventional dynamic AFM methods, amplitude and frequency modulation (AM-AFM and FM-AFM), use resonant cantilevers to intermittently and gently tap the virus while mapping material property contrast within a virus.[20,21] Nevertheless only one channel for material property contrast is available, phase lag ϕ_1 in AM-AFM[21] or dissipation channel in FM-AFM,[20] which provides scarce information to quantify material properties.

Our proposed technique (Fig. 1) *in vitro* multi-harmonic AFM exploits two important facts. On one hand the nonlinearity of the combined electrostatic/elastic/hydration forces F_{ts} between

[a]*Birck Nanotechnology Center & School of Mechanical Engineering, Purdue University, West Lafayette, IN 47907, USA. E-mail: raman@purdue.edu*

[b]*Department of Condensed Matter Physics, Universidad Autónoma de Madrid, 28049 Madrid, Spain. E-mail: p.j.depablo@uam.es*

[c]*Department of Structure of Macromolecules, Centro Nacional de Biotecnología & Instituto Madrileño de Estudios Avanzados en Nanociencia, 28049 Madrid, Spain*

† Electronic supplementary information (ESI) available: In detail theory of multi-harmonic AFM imaging in intermittent contact with sample, method validation of robustness, and additional viruses. See DOI: 10.1039/c3nr34088k

‡ These authors contributed equally to this work.

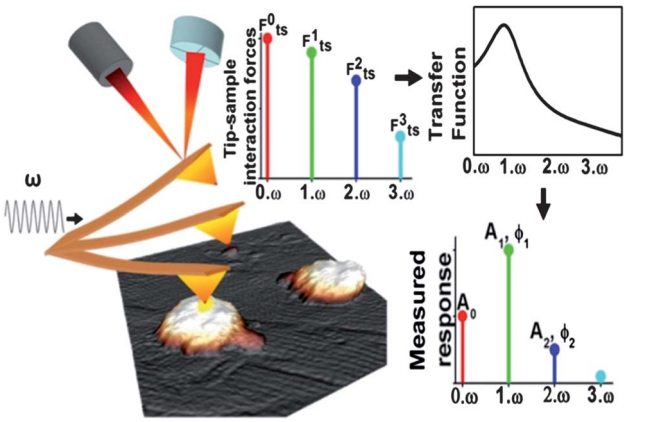

Fig. 1 Fundamentals of *in vitro* multi-harmonic AFM on viruses. A schematic of a harmonically excited (ω) cantilever intermittently interacting with a ϕ29 virion deposited on HOPG in buffer solution. Multiple tip–sample force harmonics arise at the harmonics $n\omega$, $n = 0, 1, 2, \ldots$ as a result of the nonlinear interaction forces. These forces are filtered by the cantilever transfer function resulting in significant response at the 0ω, 1ω, and 2ω harmonics of the cantilever vibration spectrum.

the tip and the virus ensures that the *in vitro* cantilever vibration spectrum features strong anharmonics of the excitation frequency ω especially at 0ω, 1ω, and 2ω. Thus these frequencies amplitudes and phases (A_0, ϕ_1, A_2, ϕ_2) boost by four-fold the available independent channels for material contrast in AM-AFM. On the other hand Lorentz-force excited AFM cantilevers in liquids have a well-defined and calibratable transfer function that can accurately relate the amplitude and phase of these cantilever harmonics to the harmonics of the tip–sample interaction forces.

Here we have studied *Bacillus subtillis* bacteriophage ϕ29 virions deposited on freshly cleaved HOPG surfaces in physiological buffer solution (see Materials and methods). The relative simplicity of phage ϕ29 has placed this virus in the spotlight of research, providing insights into the strategies used by tailed viruses.[22–24] ϕ29 is endowed with striking mechanical properties[5,14,19] which have been related to its functionality for genome storage and translocation to the host.

Materials and methods

Virus description

Bacteriophage ϕ29 is assembled in a prolate icosahedral capsid (54 × 42 nm) with a 1.6 nm thickness shell wall. The shell is made of 235 gp8 protein subunits arranged in a $T = 3$, $Q = 5$ lattice with 11 pentameric plus 20 hexameric morphological units forming icosahedral end caps, and 10 hexameric units forming the cylindrical equatorial region. The hexamers and pentamers are built by the interaction of trimers of the shell protein, each trimer building the basic triangle of the icosahedral face. The neck/tail and connector complex is 44 nm long, consists of four proteins (gp10, 11, 12 and 9), and it is held in a unique five-fold vertex of the head. Additional components of the head are the fibers made of protein gp8.5, which are dispensable for virus infectivity. The molecule of 19.8 kbp ds-DNA (6.3 μm long) is highly packed inside of the viral particle.

Sample preparation

Bacteriophage ϕ29 virions were stored in TMS buffer (10 mM $MgCl_2$, 50 mM Tris and 100 mM NaCl, 7.8 pH). A single drop of 20 μl stock solution of viral particles was deposited on freshly cleaved HOPG (ZYA quality NTMDT), and left for approximately 30 minutes. After 30 minutes the sample was washed at least 5 times with the same buffer solution. The resulting Debye length (λ_D) is ~2 to 4 nm as measured from static force–distance curves on the virus (see ESI†).

AFM imaging

In the experiments the samples were imaged in tapping mode AFM and the cantilever excited at the natural frequency. Experimental measurements of ϕ29 virions were made by using a commercial MFP-3D-BioAFM system (Asylum Research, Santa Barbara, CA, USA), and using extremely soft microcantilevers BL-TR-400PB (Olympus, Tokio, Japan) with a nominal spring constant of 0.09 N m^{-1}, $Q = 1.8$, $\omega = 8.4$ kHz, and tip radius of 50 nm that were excited using Lorentz force excitation (iDrive™) at $A_{free} \sim 4$ nm ($A_1/A_{free} = 0.8$–0.85). Lorentz force excitation directly applies an oscillating excitation force to the micro-cantilever allowing for clean phase-distortion free resonance peaks. The AFM probe is directly driven near its resonant frequency of its first frequency flexural mode and then engaged to the sample.

The ϕ29 virions deposited on HOPG in buffer solution are mounted on a MFP-3D-BioAFM for dynamic AFM imaging and material properties measurements. A custom-made cooling system was mounted inside the AFM enclosure to cool down the sample and AFM system to approximately 18 °C to create a near-physiological environment. This ensures viral capsid stability and reduces the system drift for more stable and higher resolution imaging. After the laser is properly aligned on the cantilever, the deflection sensitivity of the cantilever was calibrated by recording a static force–distance curve on freshly cleaved mica in the buffer solution to avoid tip contamination. The cantilever spring constant and quality factor of the first flexural mode was calibrated by using the thermal noise method in liquid. The excitation frequency was chosen from the peak of the tuning curve, where the phase lag becomes 90°.

For all dynamic AFM images presented in this letter, the signal acquisition and processing of multi-harmonic data were achieved using a second built-in lock-in amplifier in the MFP-3D-BioAFM controller. Unfiltered data coming from the photodiode output are then filtered using a low-pass filter with a cut-off frequency in the range of ~500 Hz. This low-pass filtered output data go into the second lock-in amplifier where the frequency to track has been set to the second harmonic (second integer multiple of the drive frequency) with a cut-off frequency of 1.5 kHz. The 0^{th} harmonic data are acquired by low-pass filtering the photodiode output below 500 Hz.

For the nanoindentation experiments an image of the virus is taken in the tapping mode in order to check the integrity of the virus and locate the center of the shell. Then, the AFM tip is moved on the top of the particle and a set of steps of 5–10 force–distance curves are acquired. After each nanoindentation assay

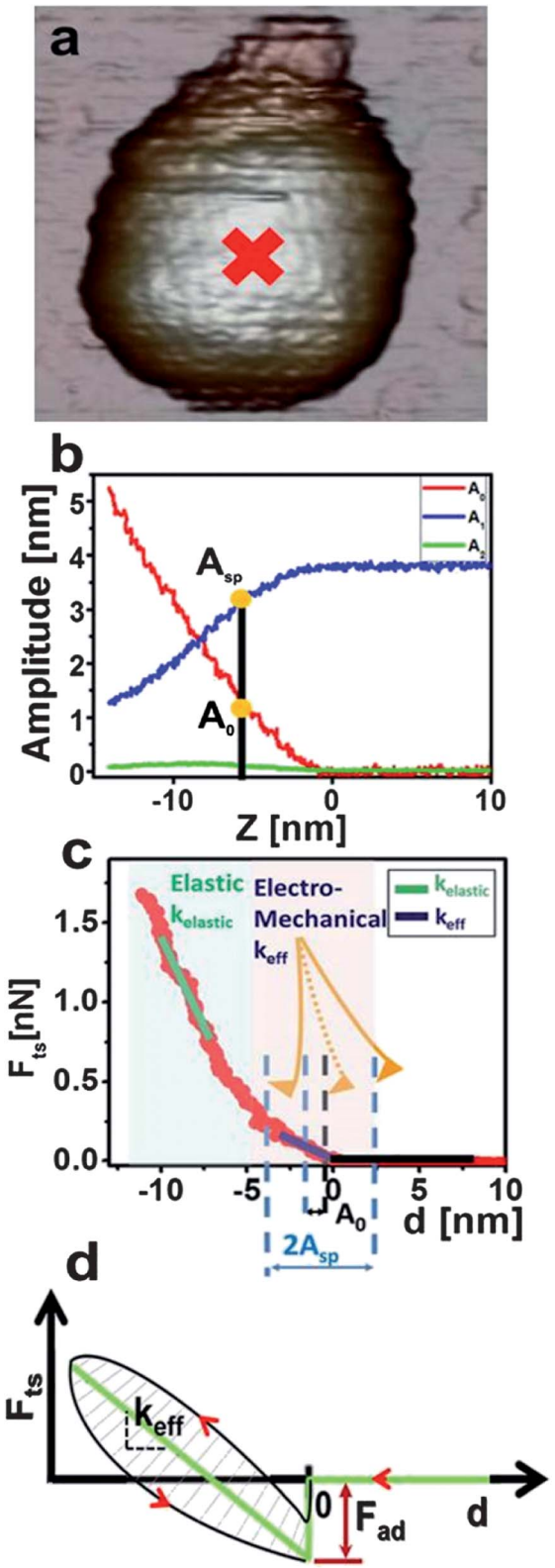

Fig. 2 (a) Topography image of a ϕ29 virion with the inset cross identifying the location where measurements were made. (b) Dynamic approach curves acquired on a location indicated by the cross in the topography image, showing the measured multi-harmonic amplitudes A_0, A_1, and A_2 (phases ϕ_1 and ϕ_2 not shown) as a function of Z. (c) By considering the Z-piezo displacement required to reduce A_1 from the unconstrained A_{1near} to the setpoint amplitude A_{sp} and noting the mean deflection (A_0) at the setpoint, it can be determined that the mean tip–sample gap d while intermittently tapping on the sample with A_{sp} is $A_{1near} - A_0$. Thus, the range of tip–sample gaps swept by the oscillating tip when scanning the virus can be determined relative to a static force *vs.* d curve acquired at the same location on the virus. Clearly the tip interacts with the virus in the gentle regime of repulsive interactions (peak force ~ <200 pN) described by an effective repulsive force gradient k_{eff} which is much smaller than the elastic stiffness $k_{elastic}$ of the particle. (d) Schematic of the simple theoretical model used to extract the unknown material properties – a repulsive gradient model with adhesion, and an added hysteresis loop representing energy dissipation due to the viscosity of the hydration layers on the sample.

a new image is recorded to check the particle integrity. All the dynamic and static approach force–distance curves recorded on the system was done using an average speed around 50 nm s^{-1} with a trigger force set around 0.8–1 nN. In the performed dynamic approach curves, the observables (A_0, A_1, A_2, ϕ_1, ϕ_2) were recorded for each curve.

Data processing

The recorded topography and multi-harmonic observable images were rendered and processed using WSxM[25] and IGOR Pro 6.2 (WaveMetrics, Lake Oswego, OR) software for optimal presentation. All computations and data processing are performed using MATLAB (The Mathworks). For each set of multi-harmonic observable (A_0, A_1, ϕ_1, A_2, ϕ_2) maps, the local effective stiffness (k_{eff}), effective viscosity (η_{eff}) and adhesive force (F_{ad}) were estimated simultaneously with nonlinear least-squared fits to the conservative and dissipative Fourier components of the interaction forces $F^0_{ts,CONS}$, $F^1_{ts,DISS}$, $F^1_{ts,CONS}$, $F^2_{ts,CONS}$, and $F^2_{ts,DISS}$. The equations used for this are presented in the ESI.†

Results

Fig. 2b shows that when resonantly excited soft AFM cantilevers approach the ϕ29 virion, the multi-harmonic observables A_0, A_1, and A_2 and their corresponding phases (not shown) are clearly detected with high signal to noise ratio. In order to link these observables to local material properties it is important to understand which interaction forces are sensed by the oscillating tip as it scans the sample. By noting the values of A_0 and Z corresponding to a typical amplitude reduction of 80–85% used for imaging, we determine (Fig. 2c) that the tip only penetrates the regime of low-force interactions with the virus (forces ~ <200 pN) which are characterized by an effective repulsive force gradient k_{eff}. This repulsive gradient can be regarded as an effective value combining the elastic stiffness of the hydrated virus $k_{elastic}$ with a force gradient k_{DLVO} due to electrostatic and van der Waals forces between the gold coated tip and the charged capsomers in the buffer solution (Debye length ~ 2 to 4 nm) *i.e.* $1/k_{eff} = 1/k_{DLVO} + 1/k_{elastic}$. We have determined (see ESI†) that under our buffer conditions the dominant contributors to k_{eff} are k_{DLVO}, which is dominated by electrostatic interactions on the virus, followed by $k_{elastic}$. Thus, k_{eff} can be regarded as the repulsive electro-mechanical force gradient sensed by the oscillating tip while scanning. Another physical property characterizing these interactions is the tip–sample adhesion force F_{ad} which depends among other factors on the local van der Waals forces and local chemical forces

(hydrophobicity/hydrophillicity) which reflect the local chemical composition of the surface. To account for energy dissipation within the hydration layers surrounding the virus, an effective viscosity η_{eff} can be introduced, representing (a) the intrinsic viscosity of a local volume of the virion, which includes both hydrated capsomers[26–28] and sub-surface DNA, and (b) the energy transfer to higher cantilever eigenmodes.[21] Thus a tip–sample force model F_{ts} describing the interactions between the AFM tip and virus particles as well as HOPG (Fig. 2d) is:

$$F_{\text{ts}} = -F_{\text{ad}} - k_{\text{eff}}(d) - \eta_{\text{eff}}\dot{d}, \text{ when } d < 0, = 0, \text{ when } d > 0$$

where the tip–sample gap is d and its time derivative is $\dot{d}$. Our interest therefore is to quantitatively map these material properties: F_{ad}, k_{eff}, and η_{eff}, within individual virions using the multi-harmonic observables.

To do so we simultaneously map the four additional observable channels A_0, ϕ_1, A_2, ϕ_2 on a ϕ29 virion while tracking its topography using AM-AFM as shown in Fig. 3a–e (data on additional viruses are provided in the ESI†). In Fig. 3, capsomer resolution is achieved in the topography on the viral capsid, collar and tail and material property heterogeneities (Fig. 3b–e) across the virus surface are clearly observed.

In order to convert the observed A_0, ϕ_1, A_2, ϕ_2 images into quantitative maps of local material properties, we have developed a perturbation theory for multi-harmonic AFM (see ESI†) which applies for the case of directly excited cantilevers (magnetic, Lorentz force, or photo-thermal excitation[29]) where a well-defined transfer function exists.[30] As we have shown the oscillating tip only intermittently taps on the viral particle, quite unlike multi-harmonic methods on live cells[31] where the tip is continuously pressed against the cell. To quantify material properties using the multi-harmonic observables in this nonlinear regime requires a significant generalization of multi-harmonic AFM theory which is presented here.

If Z is the Z-piezo displacement in an AFM and $q(t)$ is the tip displacement, then tip–sample gap is $\mathrm{d}(t) = Z + q(t)$. F_{ts}, the tip–sample-interaction force consists of a conservative (only dependent on $\mathrm{d}(t)$) and a dissipative component $F_{\text{ts,CONS}}$, $F_{\text{ts,DISS}}$, respectively, so that $F_{\text{ts}} = F_{\text{ts,CONS}}(Z + q) + F_{\text{ts,DISS}}(Z + q, \dot{q})$. The theory assumes, as seen in experiments, that the tip oscillations are dominated by the 0$^{\text{th}}$, 1$^{\text{st}}$, and 2$^{\text{nd}}$ harmonics and that F_{ts} is periodic in $\theta = \omega t - \phi_1$, so that

$$q(t) = A_0 + A_1 \sin(\theta) + A_2 \sin(2\theta + 2\phi_1 - \phi_2)$$

$$F_{\text{ts}} = F^0_{\text{ts,CONS}} + \sum_{n=1}^{\infty} F^n_{\text{ts,DISS}} \cos(n\theta) + \sum_{n=1}^{\infty} F^n_{\text{ts,CONS}} \sin(n\theta)$$

The multi-harmonic observables A_0, A_1, ϕ_1, A_2, ϕ_2 can be converted quantitatively without further assumptions using simple expressions into $F^0_{\text{ts,CONS}}$, $F^1_{\text{ts,DISS}}$, $F^1_{\text{ts,CONS}}$, $F^2_{\text{ts,CONS}}$, and $F^2_{\text{ts,DISS}}$ as shown in the ESI,† and mapped over the virus as shown in Fig. 3f–j. Striking patterns in material property heterogeneities now emerge when the experimental observables are rendered in terms of the force harmonics, not only within

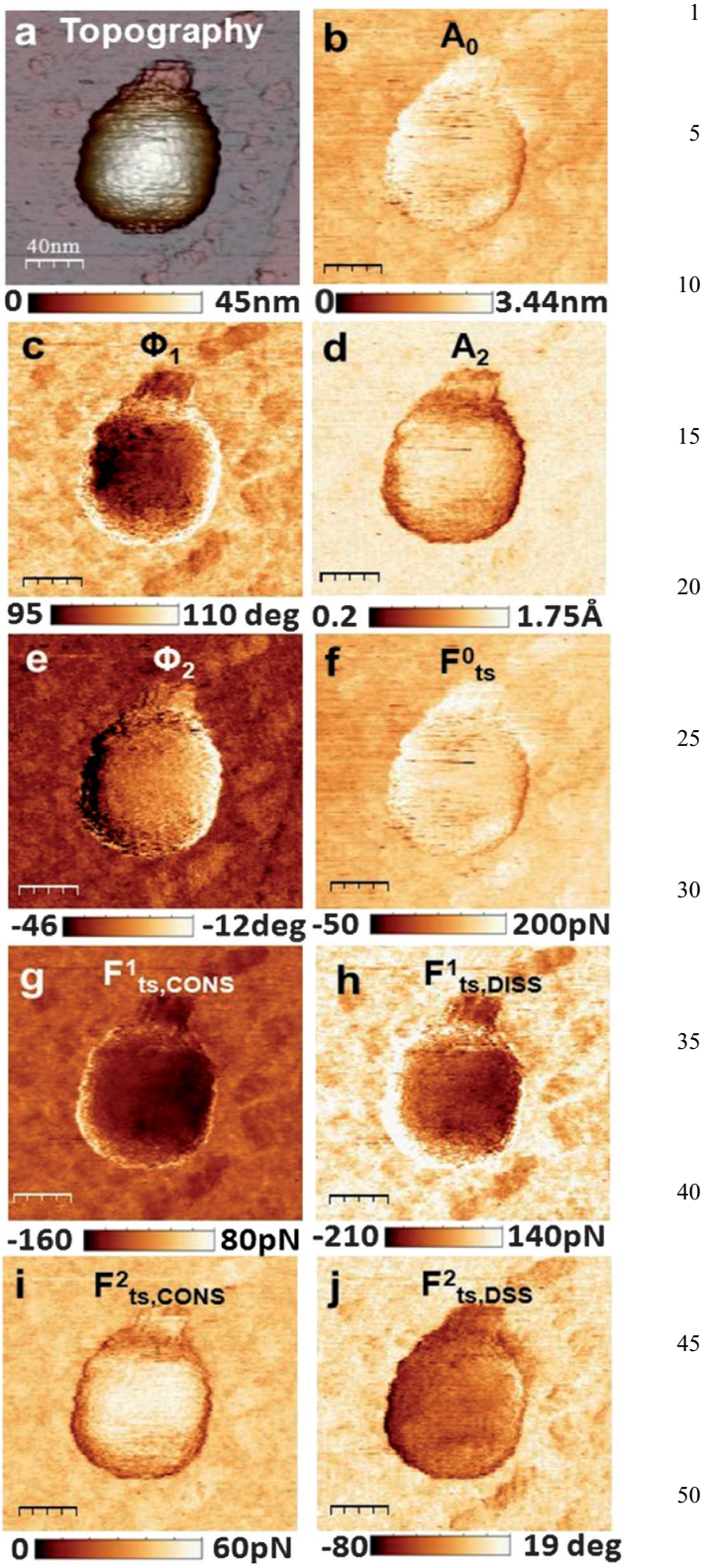

Fig. 3 Multi-harmonic observables maps. (a) Topography image acquired of a ϕ29 virion along with the multi-harmonic observable maps (unfiltered) of (b) A_0, (c) ϕ_1, (d) A_2, and (e) ϕ_2. These maps are converted using analytical formulae (ESI†) based on the transfer function of Lorentz force excited cantilevers into quantitative harmonics of the conservative and dissipative components of the interaction forces (pN), (f) $F^0_{\text{ts,CONS}}$, (g) $F^1_{\text{ts,CONS}}$, (h) $F^1_{\text{ts,DISS}}$, (i) $F^2_{\text{ts,CONS}}$, and (j) $F^2_{\text{ts,DISS}}$. Scale bar, 40 nm (size; 200 × 200 nm, pixels; 256 × 256).

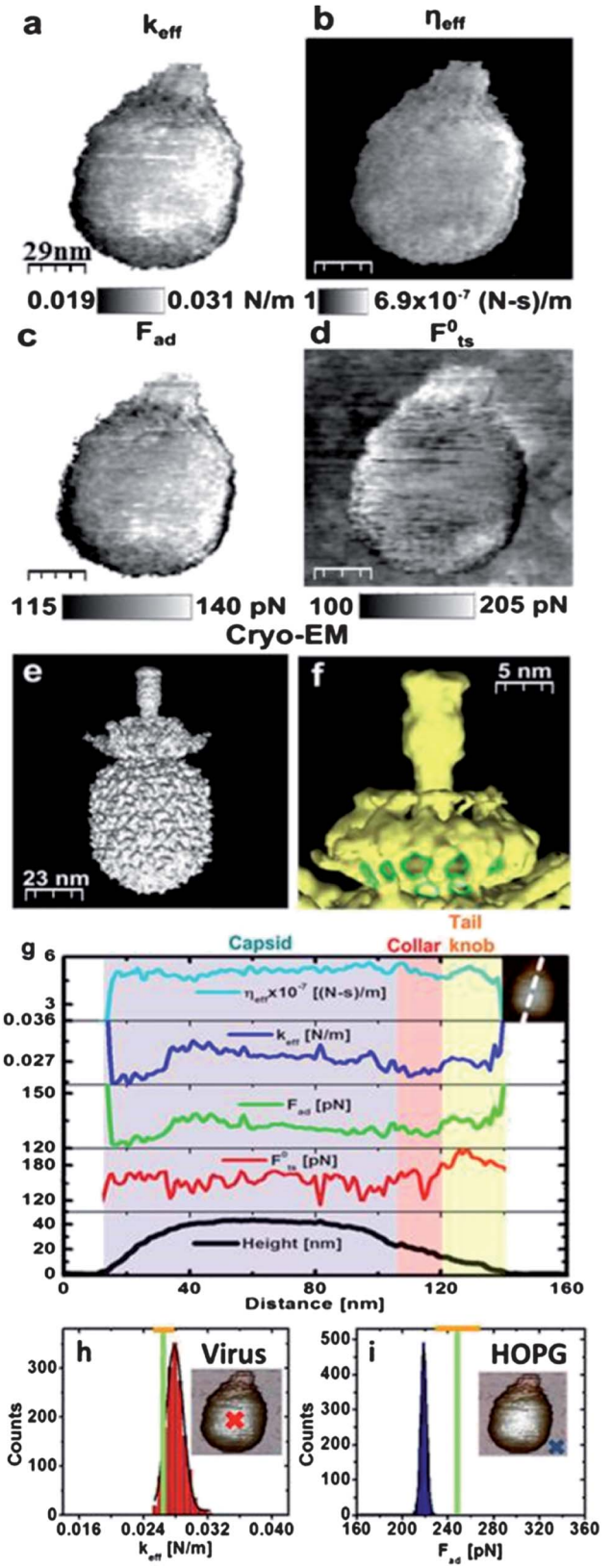

Fig. 4 Local material property maps within a ϕ29 virion and comparison with quasi-static *F*–*Z* curves. Using the analytical expressions derived in the ESI,† (a) the local electro-mechanical force gradient k_{eff} (N m^{-1}), (b) the intrinsic viscosity η_{eff} (N s m^{-1}), and (c) the adhesion force F_{ad} (pN) can be mapped over the virion (unfiltered data). In (d) the mean force map is also shown as a reference. (e) Cryo-EM predicted reconstruction of the ϕ29 virion and (f) a zoom-in image outlining cavities in the collar appendages which are well-correlated with the dark spots seen in the same region on the quantitative material property maps. (g) Line profiles of the topography and local property maps along the longitudinal axis of the virion showing many important contrasts in k_{eff} on different regions, but η_{eff} and F_{ad} remain constant. Comparison of histograms corresponding to the area in maps marked by a cross in topography insets and quasi-static *F*–*Z* curve (green and orange lines) for (h) the force gradient k_{eff} and (i) adhesion force F_{ad} (pN). Values of material property maps are within 10% of those from static *F*–*Z* curves. Scale bar AFM images, 29 nm (size; 145 × 145 nm, pixels; 256 × 256).

the viral shell and between the shell, collar, and tail but also within the collar and tail.

The quantitative measurement of a few harmonics of the interaction forces $F^0_{ts,CONS}$, $F^1_{ts,DISS}$, $F^1_{ts,CONS}$, $F^2_{ts,CONS}$, and $F^2_{ts,DISS}$ cannot be sufficient to fully reconstruct the interaction force for which many more harmonics are needed.[32–34] However since the interaction force (eqn (1)) only has a small number of unknown material property parameters, F_{ad}, k_{eff}, and η_{eff}, it is possible to quantify them from only a few force harmonics. We determine exact analytical expressions (see ESI†) that relate the measured force harmonics $F^0_{ts,CONS}$, $F^1_{ts,DISS}$, $F^1_{ts,CONS}$, $F^2_{ts,CONS}$, and $F^2_{ts,DISS}$ to the material properties F_{ad}, k_{eff}, and η_{eff}. Using these expressions, a nonlinear least-squared fit is performed pointwise on the maps to find those values of the material properties that best fit the five measured force harmonics (Materials and methods).

Fig. 4a–d show the quantitative material property maps on a single ϕ29. Fig. 4e and f provide the cryo-electron microscopy reconstruction of the ϕ29 virion,[35,36] which compare fairly well with the AFM images after taking into account the inherent tip–sample geometrical dilation.[19] Important intra-viral property contrasts, often uncorrelated to each other and to the topography, can be discerned from the maps over the capsomers, collar and tail knob protein domains. For example, the cavities formed by the appendage structure around the connector (Fig. 4f, green outlined) are clearly observed as dark spots of reduced k_{eff} (Fig. 4a–c), reflecting the local reduction in these tip–sample properties over the cavities, while η_{eff} remains relatively unchanged. From a line profile along the longitudinal axis of the virion (Fig. 4g) we observe that k_{eff} is larger on the capsid and tail but smaller on the collar while η_{eff} and F_{ad} are relatively constant. The extracted properties from the multi-harmonic method compare excellently (within 10%) of the values obtained from static force–distance curves in the virus (Fig. 4h–i). Phase contrast has been observed in these regions before[21] but the present work unambiguously relates the observed contrast to quantitative local material properties.

Our *in vitro* multi-harmonic dynamic AFM method can be applied to gain insights into the local physical properties of the ϕ29 virion after disruption. Indeed, AFM induced dismantling of viral particles has been shown to be a powerful approach to understand virus assembly/disassembly, revealing the discrete mechanical building blocks of ϕ29 prohead[37] and the intermediate kinetic assembly structures of minute virus of mice.[38] However, the material properties characterization of partially dismantled viral particles has not progressed beyond single indentation assays,[39] providing a limited understanding of the disrupted virus mechanics. Thus, our experiments consist of

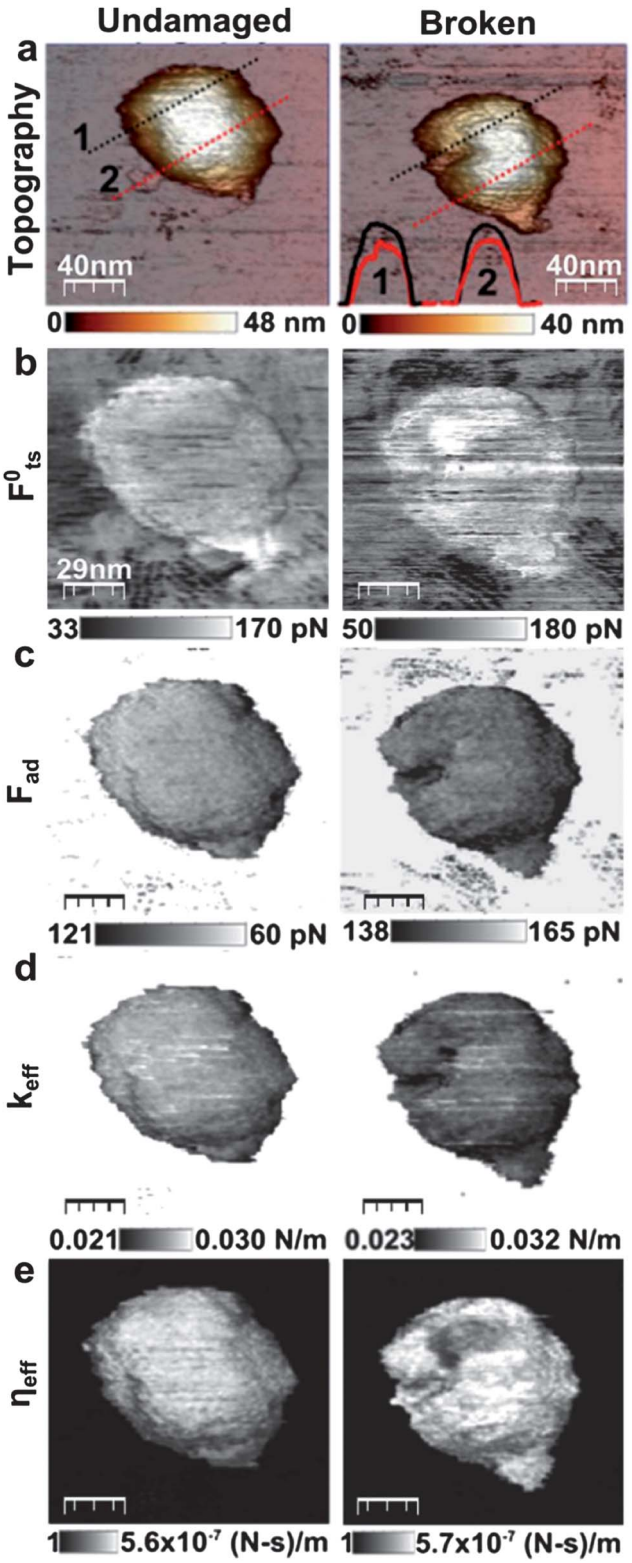

Fig. 5 AFM-induced partial disruption of the ϕ29 virion. (a) Topography image of an intact and disrupted ϕ29 virion along with the corresponding material property maps: (b) the mean force map F^0_{ts} (pN), (c) adhesion force F_{ad} (pN), (d) force gradient k_{eff} (N m^{-1}), and (e) the intrinsic viscosity η_{eff} (N s m^{-1}). In the row below the virion has been disrupted at a point by applying a point force of ~800 pN. It is clear that the local fracture of the virus shell compromises their structure integrity in intriguing ways, generating variation in topography and local properties in areas that are well removed from the damage. The insets in are line profiles of topography along the two lines, for the intact (black) and the damaged virus (red). Scale bar, 29 nm (size; 145 × 145 nm, pixels; 256 × 256).

partially disrupting ϕ29 virions by performing a nanoindentation where the maximum force is slightly higher that the breakage force[5] (Materials and methods). The multi-harmonic images before and after partial disruption were acquired and processed as described earlier (Fig. 5) demonstrating a wealth of new features within the virion. Profiles along the evidently damaged viral shell zone (lines #1) before (black) and after damage (red) shown in the insets of Fig. 5a demonstrate the expected decrease in height due to the removed capsomers.[39] However, topographical profiles (lines #2) before (black) and after damage (red), obtained along shell regions which remain undamaged, show an intriguing decrease of height that does not correspond to affected trimers.

Discussion

An in-depth analysis of these results is provided in Fig. 6, where in (a) the topography of the partially disrupted ϕ29 virion is shown with a superposed schematic representation of the icosahedral network in which the protein subunits are arranged in trimers which, in turn, build the morphologically distinct hexamers and pentamers of the intact virus. In addition, in Fig. 6c–f the difference in the topography and material properties F_{ad}, k_{eff}, and η_{eff} between the intact and disrupted virion are also shown. As can be observed in Fig. 6a the nanoindentation clearly eliminates trimer 1 and either removes or brings down trimer 2, but does not apparently further affect the remaining shell. Fig. 6c not only demonstrates the location of the directly affected shell area (trimers 1, 2, and 3), but also a homogeneous height decrease on the remaining intact shell (Fig. 6b, black), which corresponds to a volume loss of about 25%. This volume loss cannot be attributed only to the lost capsomers,[37,39] and thus must partly arise from the loss of part of the packed DNA.[35] This conclusion is consistent with prior results of internal pressurization of phage ϕ29,[14,40–42] suggesting that in Fig. 6a the virion internal pressure has been relaxed probably because the genome has been ejected. A detailed inspection of Fig. 6b–f provides further information. For instance, k_{eff} and F_{ad} decrease at removed trimers 1 and 2, while remaining nearly constant all over the intact virion shell, including trimer 3, thus indicating that the material of this shell region is the same as those of the intact trimers. As a consequence, we can infer that that trimer 3 has not been removed but pressed down. Secondly, k_{eff} decreases by ~10% over all the intact shell area, as indicated by its profile (green, Fig. 6b) along the white dotted line (Fig. 6e) map. Strikingly, the effective viscosity map (η_{eff}) (Fig. 6f) displays salient features which are not correlated with k_{eff} and F_{ad} maps (Fig. 6b, red and green curves respectively). For example, Fig. 6f clearly shows that η_{eff} decreases significantly at affected trimers 1, 2, and 3 as expected, but there are areas of the unbroken virion shell (trimer 4) that also exhibit a significant decrease in η_{eff} (Fig. 6b, blue). The energy lost to higher cantilever eigenmodes[21] is mediated by the local force gradient k_{eff} which varies little across the trimer 4

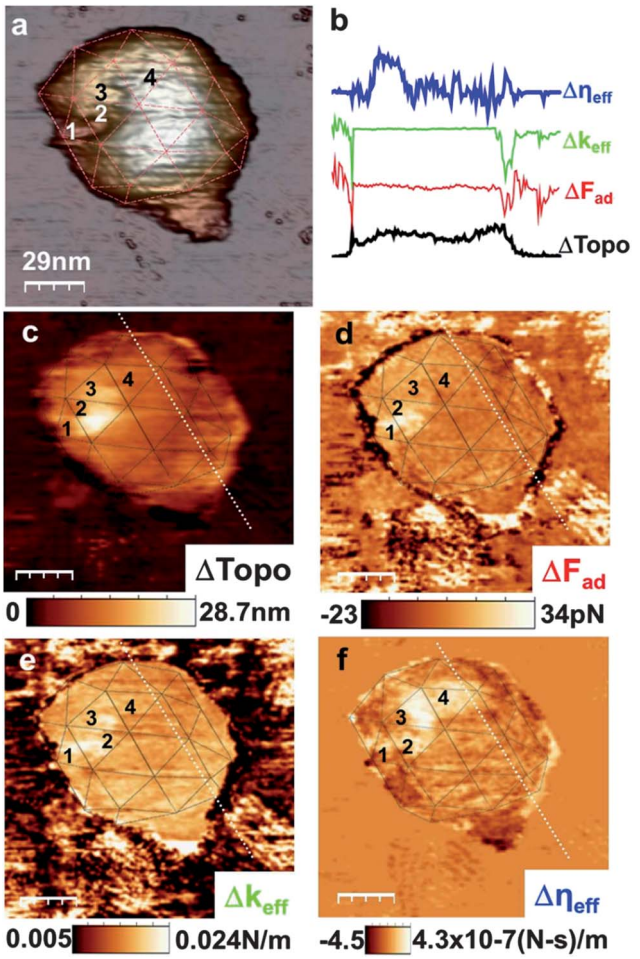

Fig. 6 Understanding material property maps within a partially disrupted virion. (a) presents the topography of a partially damaged ϕ29 virion where the capsomers network has been superposed. 4 trimers have been marked. (b) shows the profiles of (c)–(f) along the white dotted lines of each figure. (c–f) Show the differences between the intact and damaged virus in terms of F_{ad} (pN), k_{eff} (N m^{-1}), and η_{eff} (N s m^{-1}), respectively. The superimposed network enables the tracking of variations in material properties along damaged (1, 2, 3) and intact (4) trimers. Scale bar, 29 nm (size; 145 × 145 nm, pixels; 256 × 256).

(Fig. 6b, green). Therefore, the significant reduction in energy dissipation on trimer 4 is likely due to reduced viscous losses in both the hydrated shell and sub-surface DNA. Furthermore, since the shell remains intact in this region, the decrease of η_{eff} at trimer 4 must indicate a loss in the local sub-surface viscosity, possibly due to the partial ejection of hydrated viral DNA. Thus, η_{eff} maps may reveal virion areas where sub-surface dsDNA is lost due to the puncture, demonstrating that the pressurization of phage ϕ29 (ref. 14) provokes dsDNA to escape not only through the tail during infection,[41] but also through the groove left by removed capsomers. Therefore, our experiments provide a new evidence of bacteriophage pressurization, whose release partially translocates the viral DNA into the host.

Conclusions

In conclusion, we have presented a dynamic AFM technique that enables the quantitative mapping of local physical properties, including the repulsive electro-mechanical force gradient, intrinsic viscosity and adhesion at nanometer resolution within weakly bonded viruses. Our maps on partially disrupted viruses demonstrate that material properties of viruses exhibit local variations which are often uncorrelated to each other and the topography. Simultaneous mapping of multiple physical quantities enable to unveil that they do not just depend globally on the superficial viral shell, but also on local subsurface structures such as DNA. Our experimental results provide new evidence of ϕ29 pressurization showing that DNA can escape from the virion not only through the tail, but also through cracks or punctures of the viral shell. Thus, our experiments help to understand bacteriophages like pressurized vessels which can release DNA through any groove present on the viral shell. This method opens an unprecedented window to study structure–property–function relationships of viruses, nanocontainers and nanoparticles in liquid environments, which are increasingly important not only for nanomedicine and physical virology, but also to emerging applications of viruses in materials science and nanotechnology.

Acknowledgements

The authors thank the National Science Foundation Materials World Network grant DMR 1008189 "Probing *in vitro* Structure–Property–Function Relationships of Viruses at High-Resolution using Advanced Atomic Force Microscopy Methods" for financial support. Also, we acknowledge funding by grants from the Ministry of Science and Innovation of Spain, PIB2010US-00233, FIS2011-29493, Consolider CSD2010-00024 and CAM project and the Comunidad de Madrid no. S2009/MAT-1467.

Notes and references

1 J. Carter and V. Saunders, *Virology: Principles and Applications*, New Jersey, 2007.
2 P. K. Purohit, J. Kondev and R. Phillips, *Proc. Natl. Acad. Sci. U. S. A.*, 2003, **100**, 3173–3178.
3 C. Carrasco, A. Carreira, I. A. T. Schaap, P. A. Serena, J. Gómez-Herrero, M. G. Mateu and P. J. de Pablo, *Proc. Natl. Acad. Sci. U. S. A.*, 2006, **103**, 13706–13711.
4 A. Cordova, M. Deserno, W. M. Gelbart and A. Ben-Shaul, *Biophys. J.*, 2003, **85**, 70–74.
5 I. L. Ivanovska, P. J. de Pablo, B. Ibarra, G. Sgalari, F. C. MacKintosh, J. L. Carrascosa, C. F. Schmidt and G. J. L. Wuite, *Proc. Natl. Acad. Sci. U. S. A.*, 2004, **101**, 7600–7605.
6 N. Kol, Y. Shi, M. Tsvitov, D. Barlam, R. Z. Shneck, M. S. Kay and I. Rousso, *Biophys. J.*, 2007, **92**, 1777–1783.
7 J. P. Michel, I. L. Ivanovska, M. M. Gibbons, W. S. Klug, C. M. Knobler, G. J. L. Wuite and C. F. Schmidt, *Proc. Natl. Acad. Sci. U. S. A.*, 2006, **103**, 6184–6189.
8 W. H. Roos, R. Bruinsma and G. J. L. Wuite, *Nat. Phys.*, 2010, **6**, 733–743.
9 D. Peer, J. M. Karp, S. Hong, O. C. FaroKHzad, R. Margalit and R. Langer, *Nat. Nanotechnol.*, 2007, **2**, 751–760.

10 E. V. L. Grgacic and D. A. Anderson, *Methods*, 2006, **40**, 60–65.
11 T. Douglas and M. Young, *Nature*, 1998, **393**, 152–155.
12 C. B. Mao, D. J. Solis, B. D. Reiss, S. T. Kottmann, R. Y. Sweeney, A. Hayhurst, G. Georgiou, B. Iverson and A. M. Belcher, *Science*, 2004, **303**, 213–217.
13 K. T. Nam, D. W. Kim, P. J. Yoo, C. Y. Chiang, N. Meethong, P. T. Hammond, Y. M. Chiang and A. M. Belcher, *Science*, 2006, **312**, 885–888.
14 M. Hernando-Pérez, R. Miranda, M. Aznar, J. L. Carrascosa, I. A. T. Schaap, D. Reguera and P. J. de Pablo, *Small*, 2012, **8**, 2365.
15 W. H. Roos, I. Gertsman, E. R. May, C. L. Brooks, J. E. Johnson and G. J. L. Wuite, *Proc. Natl. Acad. Sci. U. S. A.*, 2012, **109**, 2342–2347.
16 X. Xu, C. Carrasco, P. J. de Pablo, J. Gómez-Herrero and A. Raman, *Biophys. J.*, 2008, **95**, 2520–2528.
17 C. Heu, A. Berquand, C. Elie-Caille and L. Nicod, *J. Struct. Biol.*, 2012, **178**, 1–7.
18 A. Ortega-Esteban, I. Horcas, M. Hernando-Pérez, P. Ares, A. J. Pérez-Berna, C. San Martin, J. L. Carrascosa, P. J. de Pablo and J. Gómez-Herrero, *Ultramicroscopy*, 2012, **114**, 56–61.
19 C. Carrasco, A. Luque, M. Hernando-Pérez, R. Miranda, J. L. Carrascosa, P. A. Serena, M. de Ridder, A. Raman, J. Gómez-Herrero, I. A. T. Schaap, D. Reguera and P. J. de Pablo, *Biophys. J.*, 2011, **100**, 1100–1108.
20 D. Martínez-Martin, C. Carrasco, M. Hernando-Pérez, P. J. de Pablo, J. Gómez-Herrero, R. Pérez, M. G. Mateu, J. L. Carrascosa, D. Kiracofe, J. Melcher and A. Raman, *PLoS One*, 2012, **7**, e30204.
21 J. Melcher, C. Carrasco, X. Xu, J. L. Carrascosa, J. Gómez-Herrero, P. J. de Pablo and A. Raman, *Proc. Natl. Acad. Sci. U. S. A.*, 2009, **106**, 13655–13660.
22 Y. Z. Tao, N. H. Olson, W. Xu, D. L. Anderson, M. G. Rossmann and T. S. Baker, *Cell*, 1998, **95**, 431–437.
23 V. Gonzalez-Huici, M. Salas and J. M. Hermoso, *Gene*, 2006, **374**, 19–25.
24 Y. R. Chemla, K. Aathavan, J. Michaelis, S. Grimes, P. J. Jardine, D. L. Anderson and C. Bustamante, *Cell*, 2005, **122**, 683–692.
25 I. Horcas, R. Fernández, J. M. Gómez-Rodríguez, J. Colchero, J. Gómez-Herrero and A. M. Baro, *Rev. Sci. Instrum.*, 2007, **78**, 013705.
26 P. Zipper and H. Durchschlag, *J. Appl. Crystallogr.*, 2007, **40**, S153–S158.
27 J. G. de la Torre, M. L. Huertas and B. Carrasco, *Biophys. J.*, 2000, **78**, 719–730.
28 S. E. Harding, *Prog. Biophys. Mol. Biol.*, 1997, **68**, 207–262.
29 D. Kiracofe, K. Kobayashi, A. Labuda, A. Raman and H. Yamada, *Rev. Sci. Instrum.*, 2011, **82**, 013702.
30 X. Xu and A. Raman, *J. Appl. Phys.*, 2007, **102**, 034303.
31 A. Raman, S. Trigueros, A. Cartagena, A. P. Z. Stevenson, M. Susilo, E. Nauman and S. A. Contera, *Nat. Nanotechnol.*, 2011, **6**, 809–814.
32 M. D. Dong, S. Husale and O. Sahin, *Nat. Nanotechnol.*, 2009, **4**, 514–517.
33 O. Sahin, S. Magonov, C. Su, C. F. Quate and O. Solgaard, *Nat. Nanotechnol.*, 2007, **2**, 507–514.
34 M. Stark, R. W. Stark, W. M. Heckl and R. Guckenberger, *Proc. Natl. Acad. Sci. U. S. A.*, 2002, **99**, 8473–8478.
35 J. H. Tang, N. Olson, P. J. Jardine, S. Girimes, D. L. Anderson and T. S. Baker, *Structure*, 2008, **16**, 935–943.
36 Y. Xiang, M. C. Morais, A. J. Battisti, S. Grimes, P. J. Jardine, D. L. Anderson and M. G. Rossmann, *EMBO J.*, 2006, **25**, 5229–5239.
37 I. L. Ivanovska, R. Miranda, J. L. Carrascosa, G. J. L. Wuite and C. F. Schmidt, *Proc. Natl. Acad. Sci. U. S. A.*, 2011, **108**, 12611–12616.
38 M. Castellanos, R. Pérez, P. J. P. Carrillo, P. J. de Pablo and M. G. Mateu, *Biophys. J.*, 2012, **102**, 2615–2624.
39 W. H. Roos, K. Radtke, E. Kniesmeijer, H. Geertsema, B. Sodeik and G. J. L. Wuite, *Proc. Natl. Acad. Sci. U. S. A.*, 2009, **106**, 9673–9678.
40 D. E. Smith, S. J. Tans, S. B. Smith, S. Grimes, D. L. Anderson and C. Bustamante, *Nature*, 2001, **413**, 748–752.
41 V. González-Huici, M. Salas and J. M. Hermoso, *Mol. Microbiol.*, 2004, **52**, 529–540.
42 W. M. Gelbart and C. M. Knobler, *Science*, 2009, **323**, 1682–1683.